HailCam: An Automated Imaging System for Real-Time Measurement of Hail Size Distributions and Fall Rates

Baolei Lyu[1,2,3], Hui ~~Wang[3]~~Wang[4], Tianlei Gao[1,2], Zhanfu ~~Yin[3]~~Yin[4], Xiaofeng ~~Lou[3]~~Lou[4], Yugang Duan[1,2], Yihang Huang[1,2], Zhiqiang ~~Zhao[3]~~Zhao[4]

[1] Huayun Sounding Meteorological Technology Co. Ltd, Beijing, 102200, China

[2] Key Laboratory of Intelligent Meteorological Observation Technology, Beijing 100081, China

[3] China Meteorological Administration Xiong'an Atmospheric Boundary Layer Key Laboratory, Xiong'an, 071000, China

[4] CMA Key Laboratory of Cloud-Precipitation Physics and Weather Modification (CPML), CMA Weather Modification Centre (WMC), Beijing 100081, China

Correspondence to: Baolei Lyu (baoleilv@foxmail.com), Hui Wang(hwang@cma.gov.cn), Zhanfu Yin (yin_zf@126.com)

设置了格式：上标

设置了格式：字体：12 磅

Abstract. Ground-based hail observations with high temporal resolution and precise microphysical quantification remain critically scarce, limiting the validation of radar-based hail detection algorithms and convective-scale numerical models. Existing automatic hail sensors often suffer from small sampling areas, susceptibility to rain interference, and limited automation in post-event processing. We present HailCam, an intelligent hail observation instrument integrating high-definition optical imaging, automated particle collection, and real-time deep learning inference to address critical gaps in time-resolved ground-based hail microphysics measurements. The system employs a ConvNeXt-Tiny architecture with Mask R-CNN for instance segmentation, capturing hailstone number, size distribution, and number flux at one-minute intervals over a 60 cm × 60 cm sampling area. Laboratory validation using synthetic ice spheres (5–45 mm) and polystyrene foam spheres demonstrates 91% sizing accuracy within ±5% relative error (RMSE 0.21–1.71 mm) and counting linearity of $R^2 = 0.9989$. Field intercomparison with an OTT Parsivel² disdrometer during a nocturnal hail event on 9 May 2025 reveals consistent temporal evolution of hailfall and statistically indistinguishable size distributions (Kolmogorov-Smirnov D = 0.167–0.250, $p > 0.84$), though absolute counts differ due to distinct phase-discrimination methodologies. HailCam provides co-located, time-stamped measurements essential for validating radar-based hail algorithms and constraining convective-scale numerical models, particularly in complex terrain where remote sensing is challenged.

1 Introduction

Hail is a highly localized yet destructive form of solid precipitation generated within intense convective storms (Allen et al., 2020). Its formation involves complex microphysical processes, wherein supercooled water droplets are lofted by strong updrafts, freeze, and undergo repeated cycles of accretion to form hailstones that eventually fall to the surface (Pflaum, 1984; Knight and Charles, 2010). Due to its sporadic occurrence, typically less than once per year at any given location in Europe (Punge and Kunz, 2016), and only two to three events per square kilometer annually even in hail-prone regions such as Switzerland (Nisi et al., 2018), hail poses significant challenges for systematic observation and climatological analysis. Accurate, high-resolution observational data on hail properties, including particle size distribution, number concentration, mass flux, and temporal evolution, are essential ~~not only~~ for understanding hail microphysics and storm dynamics~~ but~~. They also ~~for~~play a critical role in validating numerical weather prediction models (Wobrock et al., 2003), improving radar-based hail detection algorithms, and supporting risk assessment in agriculture, infrastructure, and insurance sectors (Allen et al., 2020; Martius et al., 2018).

设置了格式：字体：10.5 磅

~~Two principal~~Hail observations are generally obtained through two complementary approaches~~ are employed to observe hail,~~

~~which are~~: remote sensing techniques and ~~surface (~~in situ ground-~~truth)~~based measurements. Remote sensing techniques, primarily using weather radar, e.g., dual-polarization Doppler systems (Smyth et al., 1999; Pilorz et al., 2022), or meteorological satellites (Ravinder et al., 2013; Mroz et al., 2017), provide spatially extensive coverage and early warning capabilities. However, these methods rely on indirect proxies, such as reflectivity, differential reflectivity, or cloud-top temperature, to infer hail presence and intensity. Consequently, they suffer from inherent ambiguities and require validation against direct ground observations, especially in complex terrain where beam blockage or attenuation can degrade data quality (Skripnikova and Rezacova, 2014).

In contrast, surface-based observations offer direct, physically grounded measurements. These include manual reports from observer networks, crowdsourced data via mobile applications (Barras et al., 2019), insurance loss records (Fonseca-Cerda et al., 2026), storm chaser documentation (List et al., 2010a), drone surveys (Soderholm et al., 2020), and instrumented networks such as hailpads (Nisi et al., 2018). Among these, hailpad networks have been historically dominant due to their low cost and simplicity (Dessens et al., 2007; Sánchez et al., 2009; Changnon, 1970). Hailpads, typically made of extruded polystyrene foam, record impact craters that are later analyzed to estimate hailstone diameter under assumptions of spherical shape and constant density (Cheng and English, 1983; List et al., 2010b). Despite their widespread use, hailpads provide only time-integrated, post-event data with no information on the precise timing, sequence, or evolution of individual hail impacts, a critical limitation for studying hailfall dynamics.

To address this gap, time-resolving automatic hail sensors have emerged as a promising solution. Early prototypes, such as the hail spectrometer used by Federer and Waldvogel (1975), captured sequential images of hailstones before removal. More recent instruments include impact disdrometers (Li et al., 2024) and piezoelectric sensors that record impact timing and kinetic energy (Löffler-Mang et al., 2011; Bhandari et al., 2025). Notably, Switzerland completed in 2020 the deployment of a national network of 80 automatic hail sensors capable of timestamping individual impacts and estimating hailstone size and energy (Kopp et al., 2023a; Kopp et al., 2023b). Yet, such systems remain scarce globally, and comprehensive datasets with simultaneous measurements of hail size, count, and temporal structure are still exceptionally rare. Moreover, existing automatic sensors often face limitations, such as small sampling areas reducing statistical representativeness, susceptibility to rain interference with false positives. As climate change is projected to increase hail frequency and severity in many regions (Raupach et al., 2021; Dessens et al., 2015), the demand for robust, multi-parameter, real-time hail observation systems has been great.

In response to these challenges, we present an intelligent, deep learning–embedded hail observation instrument that integrates high-definition imaging, automated hail collection in a large sampling area with fixed time interval. By leveraging the ConvNeXt architecture for object detection, our system captures hailstone number, size distribution, and thus number flux, providing unprecedented granularity in ground-based hail characterization. This paper details the instrument design, algorithmic framework, laboratory validation, and error analysis—laying the foundation for scalable, high-fidelity hail monitoring networks. The general structure and observation principles of the instrument are described in Section 2.1, with practical realizations and workflows of the algorithms are detailed in Section 2.2. Evaluations of observation data by the instrument and related error analysis are demonstrated in Section 4.

2 Hail Intelligent Observation Algorithm and Device

2.1 Instrument Architecture and Physical Modelling Framework

The intelligent hail observation system presented in this study is designed to address three core observational gaps in current image-based hail monitoring: the lack of time-resolved hailstone counts, unfixed observation area, and limited automation in post-event data processing. To achieve these objectives, the instrument integrates mechanical collection, optical imaging, and real-time deep learning inference within a unified, weatherproof enclosure. As illustrated in Figure 1, the instrument comprises four functional modules. First, the instrument has a relatively large square collection aperture with side length = 60 cm fitted with a bar grid having 0.4 cm spacing (component 9). This grid acts as a mechanical filter: it is designed to allow rainwater and small hydrometeors (such as typical graupel and small ice pellets) to drain through, while retaining larger hail particles (⩾ 5 mm) on the grid surface for imaging.. Second, it contains an automated swiping mechanism (component 8) that conveys collected particles from the funnel base to a standardized imaging platform every minute during active precipitation. Third, a high-resolution imaging subsystem (component 10), consisting of a 8-megapixel RGB camera (pixel size = 1.55 μm) equipped with automatic low-light compensation paired with integrated diffuse LED illumination to eliminate specular reflections and ensure consistent contrast for particle segmentation even in nocturnal conditions. Lastly, ~~HailCAM~~HailCam is deployed with an NVIDIA Jetson Nano embedded computing platform, which delivers a peak AI inference performance of approximately 0.5 TOPS (trillion operations per second) under INT8 precision.

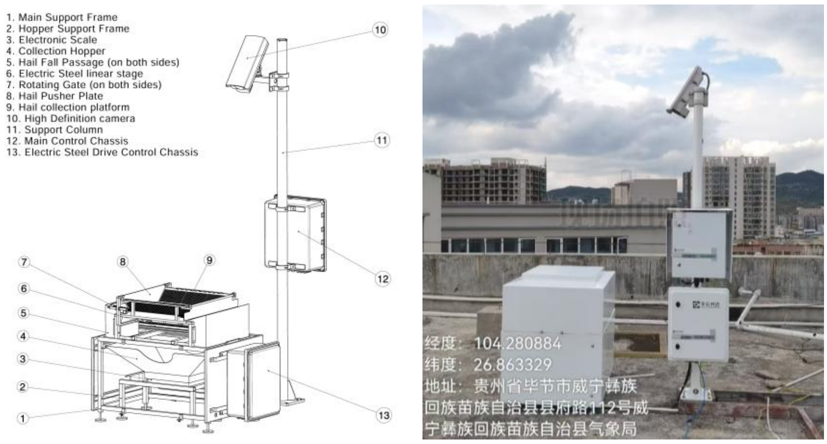

Figure 1: The major components of the hail observation device (left panel). Note: An electronic scale is installed beneath the collection tray for experimental mass validation (not used in the current automated algorithm). Photo of the HailCam deployed at the Weining Hail Suppression Experimental Base.

Unlike traditional disdrometers that infer particle size from impact momentum or acoustic signatures, our approach relies on direct geometric measurement. Each hailstone is treated as an oblate spheroid, and its projected equivalent hailstone diameter and fall rates are extracted from the binary image via deep learning segmentation.

The system operates by consecutively capturing high-resolution image on a fixed duty cycle up to 20 seconds with a default 60-second configuration, ensuring compatibility with standard meteorological reporting intervals. Specifically, it takes one single image at the 00-second mark of every sampling interval, which is 00 second in the experimental instrument in Weining. This enables continuous, unattended operation over multi-day storm sequences, a critical capability for capturing the full lifecycle of prolonged hail events. Once hailstones are detected by ~~in~~ the image processing module, HailCam ~~evacuates~~ initiates evacuation of the tray to ~~clean up~~clear the sampling area. In general, the instrument's architecture bridges the gap between passive collectors (e.g., hailpads) and high-frequency but low-fidelity impact sensors by delivering co-located, time-stamped measurements of hailstone count, and size distribution. All features are derived from physically interpretable observables rather than indirect proxies.

2.2 Deep Learning–Based Hailstone Segmentation and Characterization

Accurate identification and quantification of individual hailstones from raw imagery constitute a critical step in deriving physically meaningful microphysical parameters. Traditional computer vision approaches, such as thresholding, edge detection, or watershed segmentation, are highly sensitive to variations in lighting, surface wetness, and particle overlap, leading to substantial under- or over-counting in real-world conditions. To overcome these limitations, we implement an end-to-end deep learning pipeline based on the ConvNeXt architecture (Liu et al., 2022), which has demonstrated state-of-the-art performance in dense object detection tasks while maintaining computational efficiency suitable for edge deployment.

2.2.1 Network Architecture and Training Protocol

The core of our algorithm is a modified ConvNeXt-Tiny backbone integrated with a Feature Pyramid Network (FPN) head for multi-scale feature fusion, followed by a Mask R-CNN–style instance segmentation head. This architecture implements a hierarchical feature learning strategy to address the challenges of dense hail detection.

First, the ConvNeXt-Tiny backbone employs a modern ConvNet design with large convolutional kernels and a LayerNorm-centric architecture. It processes the input image through multiple stages, progressively extracting semantic features while reducing spatial resolution. ~~This provides a robust foundation for visual representation learning.~~ Given an input RGB image $I \in R^{3\times H\times W}$, feature extraction is performed using the ConvNeXt-Tiny backbone. The backbone consists of four hierarchical stages with downsampling ratios of 4, 8, 16, and 32, producing multi-scale feature maps C_1, C_2, C_3, C_4. These representations provide progressively increasing receptive fields, where shallow layers preserve fine spatial detail and deeper layers encode high-level semantic context.

Second, the Feature Pyramid Network (FPN) is applied to the outputs of the ConvNeXt backbone. The FPN constructs a pyramid of feature maps by top-down lateral connections. This mechanism allows the fusion of strong semantic information from deeper layers with high-resolution spatial details from shallower layers. ~~Consequently, the model achieves scale invariance, enabling accurate detection of hailstones ranging from small fragments to large aggregates.~~ Specifically, each feature map $\boldsymbol{C_i}$ is first transformed using a 1×1 convolution to obtain a uniform channel embedding $L_i = \mathrm{Conv}_{1\times1}(C_i)$. top-down pathway then progressively upsamples higher-level features and fuses them with corresponding lateral features via element-wise addition $T_i = L_i + \mathrm{Upsample}(T_{i+1})$. A 3×3 convolution is subsequently applied to each fused feature map to suppress aliasing and refine spatial consistency, yielding the final pyramid features $P_i = \mathrm{Conv}_{3\times3}(T_i)$.The resulting feature pyramid P_1, P_2, P_3, P_4 provides strong multi-scale representations for both small and large hailstones.

Finally, the Mask R-CNN–style head operates on this fused feature pyramid to perform instance segmentation. ~~It utilizes a Region Proposal Network (RPN) to generate candidate object bounding boxes.~~The FPN outputs serve as inputs to a Mask R-CNN-based instance segmentation module. A region proposal network (RPN) generates candidate hailstone regions from the fused feature maps. For each proposal, RoI Align is applied to extract fixed-size region features while preserving spatial alignment. For each candidate region, the network branches into three parallel outputs: (1) a classifier to confirm the presence of hail, (2) a regressor to refine the bounding box coordinates, and (3) a Fully Convolutional Network (FCN) mask branch that predicts a binary segmentation mask for the hailstone at pixel resolution. This allows the system to distinguish individual hailstones even in scenarios of slight overlap, providing precise geometric boundaries for diameter calculation.

~~This configuration enables simultaneous prediction of bounding boxes, semantic masks, and confidence scores for each detected hailstone.~~ The input to the network is a 640×640-pixel RGB image captured under controlled diffuse illumination. The instance segmentation outputs are further used for quantitative hail characterization.

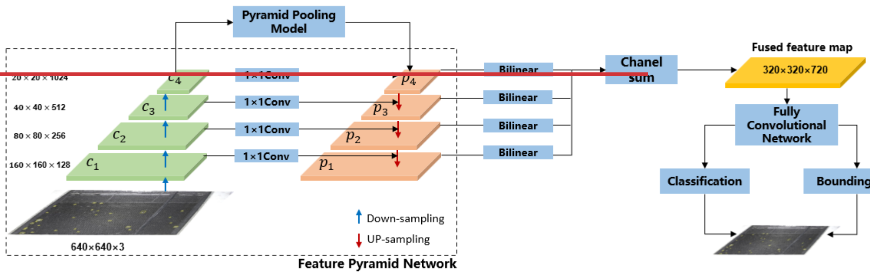

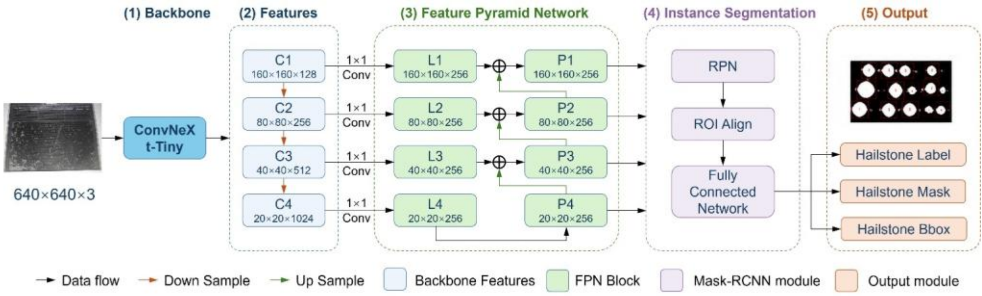

Figure 2: work flow of model detection algorithm.

2.2.2 Model Hyperparameters and Training

Training data were generated from a curated dataset of 8,742 manually annotated ~~images~~instances collected during the hail season in 2024, encompassing diverse hail morphologies (spherical, conical, irregular), sizes (5–45 mm equivalent diameter), and surface conditions (dry, wet, partially melted). Specifically, the full dataset of 8,742 images is split into training set: 70% (6,119 images), validation set: 15% (1,311 images) and testing set: 15% (1,312 images). The split is performed at the image level with random stratification to ensure balanced hail size and density distributions across subsets. The validation set is used exclusively for early stopping, while the test set is strictly held out for final performance evaluation.

The model hyperparameters are shown in the following Table 1. To enhance robustness, we applied photometric augmentations (e.g., random brightness/contrast shifts) and geometric transformations (rotation, scaling, elastic deformation) during training. The model was optimized using the AdamW optimizer with a cosine-annealed learning rate (initial = 3×10^{-4}) and a composite loss function combining focal loss for classification, smooth L1 loss for box regression, and Dice loss for mask refinement. Crucially, the deep learning approach eliminates the need for manual tuning of segmentation thresholds, adapts dynamically to changing environmental conditions, and achieves a high particle detection accuracy.

Table 1 The hyperparameters in our model.

Hyperparameter	Ours
Data augmentations	photometric augmentations, geometric transformations
Batch size	4
FPN channel size	256
Optimizer	AdamW
Scheduler	Cosine Annealing, $\eta_{max}= 3\times10^{-4}$, $\eta_{min}= 0$, $T_{max} = 50$
Training epochs	up to 100 with early stopping patience = 10
Weight decay	1×10^{-3}

2.2.~~2~~3 Model Inference and Post-Processing

During operational inference, the trained model processes each one-minute image frame in real time on an embedded GPU (NVIDIA Jetson Nano). Detected instances with a confidence score below 0.7 are discarded to suppress false positives from water droplets, debris, or imaging artifacts. Overlapping detections (IoU > 0.5) are resolved via non-maximum suppression (NMS), ensuring one-to-one correspondence between physical particles and predicted masks.

To recover the physical dimensions of each segmented retained instance within the imaged hail collection tray, we formulate the problem as a metric reconstruction from a single calibrated perspective view. The tray contains a known square reference pattern of side length L, lying on the plane Z=0 of the world coordinate system. Given the camera's intrinsic matrix $\boldsymbol{K}$ and extrinsic parameters ($\boldsymbol{R}$,$\boldsymbol{t}$)—obtained via prior calibration—we compute the homography $\boldsymbol{H}$ that maps points on this plane to image pixels:

$$\boldsymbol{H} = \boldsymbol{K}\cancel{[\boldsymbol{r}_1 \boldsymbol{r}_2 \boldsymbol{t}]}[\boldsymbol{r}_1 \boldsymbol{r}_2 \boldsymbol{t}] \qquad (1)$$

where $\boldsymbol{r}_1, \boldsymbol{r}_2$ are the first two columns of the rotation matrix $\boldsymbol{R}$. The four corners of the region of interest are detected in the image as $\boldsymbol{p}_i \cancel{= (u_i, v_i)^t (i = 1, \ldots, 4).} = (u_i, v_i)^t (i = 1, \ldots, 4)$. After correcting for lens distortion, these points are back-projected onto the Z=0 plane using $\boldsymbol{H}^{-1}$, yielding their metric coordinates $\cancel{(X_i, Y_i).}(X_i, Y_i)$. The real-world width and height are then obtained via Euclidean distances between corresponding corner pairs. This approach enables pixel-to-millimeter conversion with sub-millimeter accuracy. In cases where extrinsic parameters are unknown, they can be estimated by solving a Perspective-n-Point (PnP) problem using the detected corners of the full reference square, as detailed in the Text S1 in the Supplementary Material.

For each retained instance, hailstone diameter could be obtained under the assumption that hailstone is a standard sphere. The equivalent diameter D_i in physical units (mm) is then derived as:

$$\cancel{D_i = \frac{|X_{i,left} - X_{i,right}| + |Y_{i,top} - Y_{i,bottom}|}{2}} \boldsymbol{D_i} = \frac{|\boldsymbol{X_{i,left} - X_{i,right}}| + |\boldsymbol{Y_{i,top} - Y_{i,bottom}}|}{\boldsymbol{2}} \qquad (2)$$

While this assumes spheric shape, a simplification that introduces bias for highly elongated or fragmented stones, it aligns with standard practice in optical disdrometry and provides consistency with radar-based size definitions, e.g., maximum dimension in dual-polarization retrievals (Skripnikova and Rezacova, 2014).

2.3 Experimental Validation and Uncertainty Quantification

To establish the metrological credibility of the intelligent hail observation system, we conducted a multi-stage validation protocol encompassing controlled laboratory experiments, and side-by-side field intercomparisons. This section details the experimental design for key observables: hailstone count, and equivalent diameter.

2.3.1 Laboratory Calibration with Artificial Hailstones

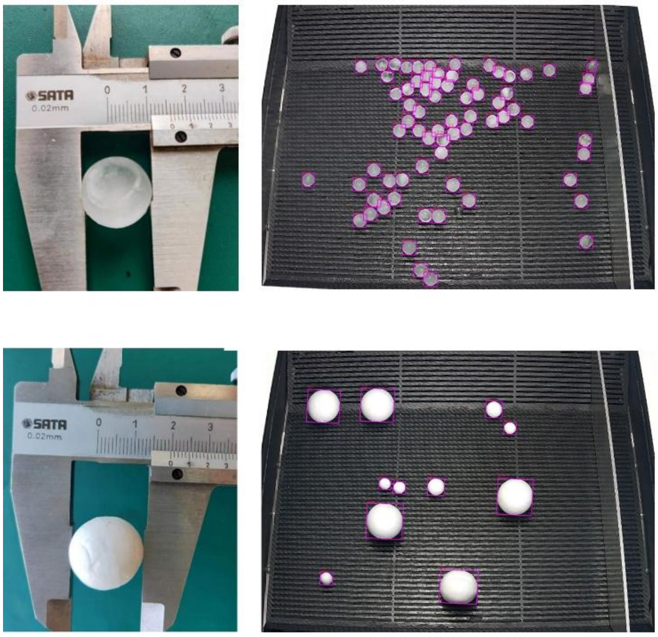

Figure 3: Balls of the same material and size placed in batches with different quantities on the equipment to calculate the average diameter.

Due to the inherent unpredictability of natural hail events in terms of timing, location, and intensity, laboratory-based validation experiments were conducted to quantitatively assess the measurement accuracy of the HailCam system. Two complementary experimental protocols were designed to independently evaluate the instrument's sizing and counting capabilities.

Synthetic hailstones were fabricated using distilled water frozen in spherical molds under controlled laboratory conditions. Seven nominal diameter classes were produced: 5, 7.5, 10, 15, 20, 35, and 45 mm, encompassing the typical size range observed in mid-latitude severe storms (Nisi et al., 2018). For each size class, 50 ice spheres were randomly dropped onto the collection tray. The automated imaging pipeline subsequently captured and processed the projected silhouettes of these particles. The instrument-derived equivalent diameters were compared against the reference diameters measured using a precision digital caliper (±0.01 mm accuracy) to quantify sizing accuracy and precision across the operational range.

To assess the system's quantification accuracy under varying particle number densities, expanded polystyrene foam spheres of mixed diameters (ranging from 5 to 30 mm) were employed as proxy hailstones. A total of 96 independent trials were conducted, with each trial involving the manual placement of 3 to 250 foam spheres on the collection tray in randomized spatial configurations. This range was selected to evaluate performance from sparse distributions (representative of marginal hailfall conditions) to dense accumulations (approaching the upper limit of typical hailstorm intensities). The automated detection algorithm processed each image frame, and the retrieved particle counts were compared against the ground-truth counts established through manual enumeration.

The ice sphere experiments specifically targeted sizing fidelity under controlled morphological conditions, while the foam sphere trials focused on counting accuracy across a broad dynamic range of particle concentrations. The combination of these two protocols enables comprehensive characterization of both the metrological traceability of individual particle measurements

带格式的: 段落间距段后: 8 磅, 行距: 多倍行距 1.16 字行, 到齐到网格

and the statistical robustness of population estimates derived from the imaging system. Static manual placement of artificial ice and foam spheres was selected to isolate optical imaging and instance segmentation errors without confounding impact fragmentation or deformation effects. These laboratory results define the minimum achievable measurement uncertainty under idealized particle conditions. Actual total field uncertainty will incorporate additional error contributions from high-speed hail impacts, shape distortion, and fragmentation unquantified in this static framework.

2.3.2 Field Intercomparison with Reference Instruments

To evaluate the performance of the HailCam system under complex natural climatic, topographic and illumination conditions, co-located field intercomparisons were conducted at the Weining Hail Suppression Experimental Base of the China Meteorological Administration (CMA), located in Guizhou Province (26.9°N, 104.9°E), as shown in Figure 1. This study area is characterized by typical karst terrain with rugged relief and frequent severe convective weather, posing rigorous practical tests for the stability, anti-interference and detection accuracy of hail observation instruments in complex underlying surface environments.

A co-located OTT Parsivel² laser disdrometer (hereinafter referred to as disdrometer) was deployed alongside the HailCam system as the reference instrument. The disdrometer is a widely utilized optical precipitation spectrometer that measures particle size distributions and fall velocities based on the extinction of a horizontal laser beam by hydrometeors passing through the sampling area (Loffler-Mang and Joss, 2000). The OTT Parsivel² has a nominal size accuracy of ±1 bin (approximately ± 0.125 mm for small particles, scaling non-linearly) under laboratory conditions, though field accuracy can be affected by turbulence and alignment (Tokay et al., 2014). The device provides size distributions across 32 diameter classes ranging from 0.062 to 24.5 mm, and has been widely used reference instrument for hydrometeor particle size and fall velocity measurement (Tokay et al., 2014; Loffler-Mang and Joss, 2000). The disdrometer was set to its standard operational mode with a 1-minute sampling interval, consistent with the default data acquisition frequency of HailCam, to enable direct temporal and quantitative comparison of observational data.

A particularly valuable validation opportunity arose during a rare nocturnal multi-pulse hail event on 9 May 2025 at approximately 22:00-24:00 Beijing Time (UTC+8). This event featured two distinct hail pulses with maximum hailstone diameters of 5–20 mm, falling over a cumulative duration of 16 minutes under low-light conditions, representing a challenging scenario for optical detection systems. The disdrometer recorded continuous particle size distributions throughout the event, enabling direct comparison with HailCam's imaging-based measurements. The intercomparison focused on three quantitative metrics, including temporal correlation of hailfall detection and intensity variations, consistency of particle number concentrations (particles m^{-2} min^{-1}), and agreement of hailstone size distributions. To ensure a consistent comparison with HailCam which mechanically filters particles < 5 mm via its collection grid, we specifically selected disdrometer data for particles with an equivalent diameter ≥ 5 mm for all statistical analyses. This intercomparison with the disdrometer's established optical disdrometry capabilities provides a robust framework for assessing the accuracy and reliability of the novel imaging system under operational field conditions. The detailed intercomparison results are presented in Section 3.2.

3. Results and Discussions

3.1 Laboratory Evaluation

3.1.1 Ice Sphere Sizing Accuracy

To quantitatively assess the sizing fidelity of HailCam, we performed controlled calibration experiments using synthetic ice spheres across seven nominal diameter classes (5, 7.5, 10, 15, 20, 35, and 45 mm). For each size class, 50 ice spheres were individually introduced onto the collection tray, and their projected silhouettes were captured and processed by the automated imaging pipeline.

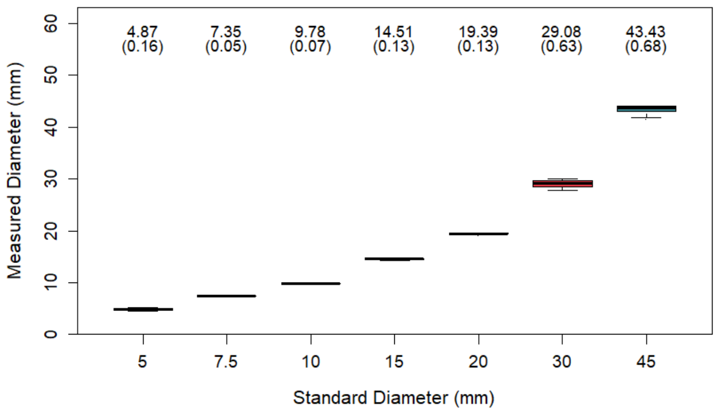

Figure 4: Boxplot of measured hailstone diameters from HailCam versus seven standard reference sizes (5–45 mm). For each size class, 500 artificial ice spheres were individually introduced into the collection tray and automatically sized by the imaging system. The mean measured diameter and standard deviation (in parentheses) are ~~labeled~~labelled above each box.

Figure 4 presents boxplots of the measured diameters versus the reference sizes. The system exhibits high repeatability but a systematic negative bias: the mean measured diameters are consistently smaller than the true values, with relative errors ranging from approximately 1.97% at 7.5 mm to 3.63% at 15 mm~~.~~ (Table 2). This underestimation arises primarily from incomplete particle contour detection, where inter-particle occlusion leads to partial loss of edge information. Additionally, the standard deviation associated with each size class captures not merely random measurement noise but also spatial heterogeneity of measurement performance across the collection area. Particles landing away from the optical center experience subtle variations in lighting and viewing angle, contributing to the observed spread in measured diameters even for identical reference spheres.

Table ~~1:~~2: The statistic metrics for evaluating hailstone diameter mean.

Standard Diameter (mm)	**5**	**7.5**	**10**	**15**	**20**	**30**	**45**
Accuracy (relative error ⩽5%)	72%	100%	100%	92%	98%	88%	84%
RMSE (mm)	0.21	0.15	0.23	0.57	0.62	0.95	1.71
MB (mm)	-0.13	-0.15	-0.22	-0.54	-0.61	-0.81	-1.57
NMB	-2.68%	-1.97%	-2.21%	-3.63%	-3.03%	-2.70%	-3.48%

Despite these effects, the overall accuracy remains sufficient for microphysical classification: 91% of measurements for particles fall within ±5% of the true diameter. The root-mean-square error (RMSE) increases monotonically with particle size, from 0.21 mm (5 mm class) to 1.71 mm (45 mm class), consistent with the fixed-pixel resolution of the imaging system (1.55 µm pixel size, 8-megapixel sensor). This level of precision supports reliable estimation of derived quantities such as hail kinetic energy (which scales with D^3) and number concentration, both critical for severe storm nowcasting and radar algorithm validation.

3.1.2 Foam Sphere Counting Accuracy

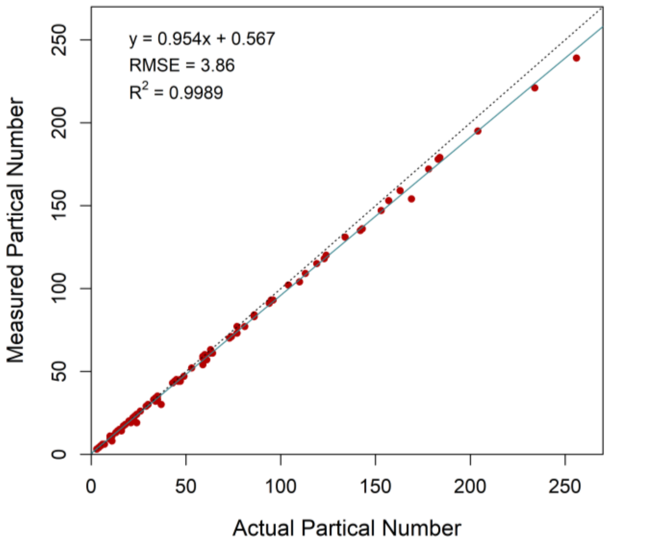

Figure 5: Scatter plot of measured versus actual hailstone counts from 94 controlled calibration experiments.

To evaluate the quantification accuracy of HailCam across varying particle number densities, we conducted 96 independent trials using expanded polystyrene foam spheres of mixed diameters (5–20 mm). Each trial involved manual placement of 3 to 250 spheres on the collection tray in randomized spatial configurations, spanning the operational range from sparse distributions (representative of marginal hailfall) to dense accumulations (approaching high-intensity hailstorm conditions). Figure 5 displays the scatterplot of measured versus actual particle counts. The results reveal a strong linear relationship (R^2 = 0.9989), indicating that over 99.8% of the variance in measured counts is explained by the true values. The fitted regression line y = 0.954x + 0.567 exhibits a slope close to unity (0.954) and a small positive intercept (0.567), confirming near-proportional response across the full measurement range. The RMSE of 3.86 particles corresponds to a relative error of 4.0% for counts >100 and 2.8% for small groups (<100 particles). Minor undercounting, particularly evident at higher densities (>150 particles), is attributed to the reason that in dense clusters, overlapping particles can obscure edges, leading to merged contours or incomplete segmentation by the ConvNeXt algorithm. Notably, the absence of significant outliers or non-linear trends suggests robust algorithmic performance across variations in particle spatial distribution.

3.2 Field Evaluation

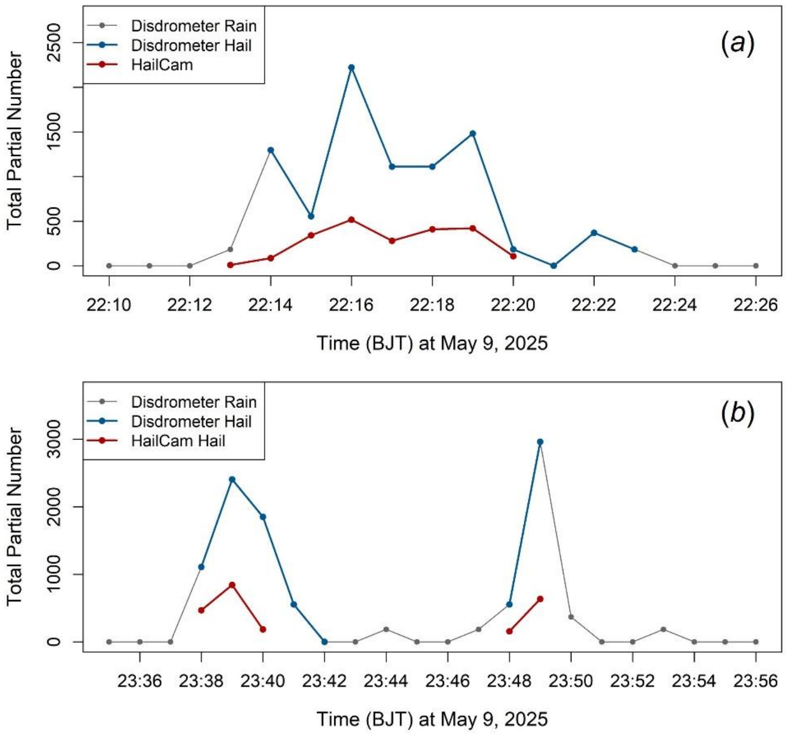

Figure 6: Temporal evolution of total particle number with diameters ≥5 mm are considered. detected by the OTT Parsivel² disdrometer and HailCam during two hail episodes on 9 May 2025. (a) First hail episode (22:13–22:20 BJT) and (b) second hail episode (23:38–23:49 BJT). The disdrometer data are disaggregated into rain (grey) and hail (blue) components based on the instrument's classification algorithm, while HailCam measurements (red) represent hail particles with equivalent diameters ≥5 mm. Note the different scales on the y-axes between panels (a) and (b).

On 9 May 2025, the HailCam system recorded two distinct hailfall episodes during a nocturnal convective event at the Weining site, revealing pronounced intra-storm variability in intensity, duration, and microphysical structure. The first episode initiated at approximately 22:14 BJT and persisted for ~12 minutes, exhibiting a multi-peaked structure with maximum particle counts reaching 2,200 min^{-1} recorded by the disdrometer and 516 m^{-2} min^{-1} by HailCam at 22:16 BJT (Figure 6a). The second episode, including two pulses occurring from 23:38 to 23:40 BJT and from 23:48 to 23:49 BJT, displayed even higher peak intensities, with the disdrometer detecting >2,800 particles min^{-1} and HailCam measuring 844 m^{-2} min^{-1} at 23:39 BJT (Figure 6b).
Comparison of the two instruments reveals both consistencies and notable discrepancies. Temporally, both systems capture the onset, peak, and cessation of hailfall with good agreement, confirming HailCam's capability to resolve the fine-scale evolution of hail events. However, substantial differences in absolute particle counts are evident: the disdrometer consistently reports 3–5 times higher total particle numbers than HailCam throughout both episodes. This discrepancy arises from fundamental differences in measurement principles and sampling geometries. The disdrometer's horizontal laser beam (30 mm wide, 180

mm long) captures all hydrometeors passing through the sampling volume, including small ice fragments, graupel, and raindrops. In contrast, HailCam's imaging-based approach applies stricter criteria (solid-phase classification via deep learning, minimum 5 mm diameter threshold, and morphological validation), thereby excluding smaller or partially melted particles and large rain drops that may be counted by the disdrometer.

Figure 7: Sample image of the three hail episodes captured at Weining station.

The image captured by HailCam at three time points are shown in Figure 7. The observed concentration of hail in the lower left quadrant (Figure 7) is attributed to aerodynamic drag and prevailing wind direction within the collection funnel during the measurement. This spatial bias reduces the effective sampling area compared to a uniform distribution. According to the laboratory tests for counting accuracy in Section 3.1.2, we estimate this could introduce a systematic uncertainty of up to 5% in the calculated concentration density due to edge effects and potential particle overlap in the compressed area. Furthermore, the disdrometer's "hail" classification (blue dots in Figure 6) relies on empirical fall velocity thresholds, which can misidentify large raindrops or conical graupel as hail, particularly during periods of mixed-phase precipitation. This is evident in Figure 6a during the interval 22:20–22:24 BJT, where the disdrometer continues to register substantial "hail" counts while HailCam detects minimal solid precipitation, suggesting possible misclassification of heavy rain or melting particles. Conversely, HailCam's negative bias may partially result from reasons that the 60-second imaging duty cycle potentially missing brief, intense sub-minute fluctuations. Besides, particle overlap on the collection tray during peak intensities causing under-segmentation also lead to negative observation bias.

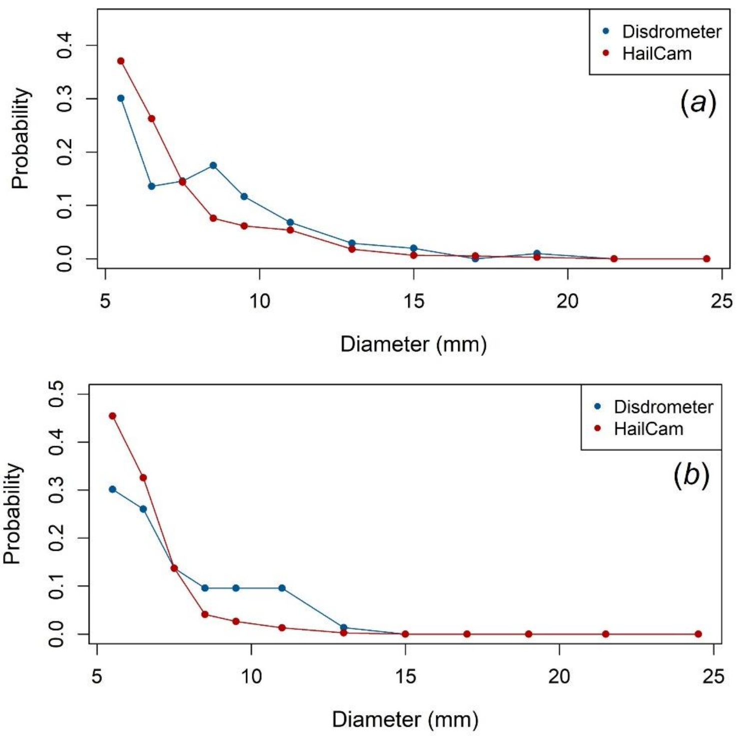

Figure 8: Probability density functions of hailstone equivalent diameters measured by HailCam (red circles) and the OTT Parsivel² disdrometer (blue circles) for the two hail episodes on 9 May 2025. (a) First episode (22:13–22:20 BJT) and (b) second episode (23:38–23:49 BJT). Diameter bins are 1 mm wide, and probabilities are normalized by the total number of particles ≥5 mm detected by each instrument during the respective time periods.

The hailstone size distributions (HSDs) derived from HailCam and disdrometer observations exhibit distinct patterns that reflect fundamental differences in measurement principles (Figure 8). For the first episode (Figure 8a), HailCam records a sharp dominant peak at 5–6 mm with probability 0.36, followed by a rapid monotonic decrease toward larger sizes. In contrast, the disdrometer distribution is bimodal, with a primary peak at 5–6 mm (probability 0.30) and a pronounced secondary peak at 8–9 mm (probability 0.17). Notably, the disdrometer detects substantially higher probabilities in the 7–11 mm range, while HailCam shows enhanced probabilities only at the smallest bin (5–6 mm).

The second episode (Figure 8b) displays even more pronounced divergence between the two instruments. HailCam again exhibits a unimodal distribution peaked sharply at 5–6 mm (probability 0.45), with near-zero probabilities beyond 12 mm. The disdrometer, however, shows a much flatter distribution with a primary peak at 5–6 mm (probability 0.30), a secondary peak at 7–8 mm (probability 0.26), and sustained probabilities of ~0.10 across the 8–12 mm range. ~~This discrepancy suggests that the disdrometer's velocity-based classification algorithm may be misidentifying larger raindrops or graupel particles as hail, whereas HailCam's imaging-based segmentation strictly enforces morphological criteria for solid-phase identification.~~

A widely adopted theoretical framework for describing hydrometeor size spectra, including hail, is the gamma distribution, which typically features a probability density function that rises to a distinct intermediate-size peak before decaying exponentially (Wang et al., 1987). Neither instrument's HSD fully conforms to this canonical gamma shape across the two observed hail episodes. HailCam produces a strictly unimodal, monotonically decreasing exponential distribution with a dominant peak confined to the smallest 5–6 mm bin and negligible probabilities for diameters >12 mm, while the Parsivel² disdrometer exhibits a weak secondary probability hump near 7–9 mm but still lacks a pronounced gamma-mode peak at larger sizes. A key limiting factor for recovery of a classical gamma HSD is the limited observational sample size: our analysis draws exclusively from two short-duration nocturnal hail pulses on a single storm night, with relatively limited total hail particle counts compared to multi-event, multi-storm climatological datasets used to derive gamma distribution parameters in prior literature. Beyond limited sampling, the fixed 60-second imaging duty cycle of HailCam introduces a melting bias: hailstones collected on the sampling grid sit exposed to ambient near-freezing air for up to 60 s before automated imaging, leading to partial surface ablation that reduces measured equivalent diameter and further shifts mass and particle counts toward the smallest 5–6 mm bin.

Quantitative comparison reveals no statistically significant differences between the two instruments at conventional confidence levels. Kolmogorov-Smirnov tests yield $D = 0.167$ ($p = 0.996$) for the first episode and $D = 0.250$ ($p = 0.848$) for the second episode, indicating failure to reject the null hypothesis of identical distributions. Despite the visual divergence in distribution shapes, particularly the disdrometer's enhanced probabilities in the 7–12 mm range, the cumulative distribution functions are sufficiently similar that the observed differences may plausibly arise from sampling variability rather than systematic measurement bias. This statistical indistinguishability suggests that both instruments capture the same underlying hail population, albeit with different detection efficiencies across the size spectrum. The disdrometer's broader tails likely reflect inclusion of marginal ice-phase particles that satisfy its velocity-based criteria, while HailCam's sharper concentration at small sizes indicates more stringent morphological filtering.

These findings have important implications for operational applications. The agreement in cumulative distributions validates HailCam as a reliable alternative to established disdrometry for hail characterization, particularly given its superior phase discrimination capabilities. While the disdrometer provides continuous high-temporal-resolution measurements, its velocity-based classification may introduce uncertainty in phase identification that HailCam's imaging approach mitigates through direct morphological validation. The complementary strengths of the two instruments, disdrometer sensitivity to the full hydrometeor population and HailCam specificity for unambiguous solid hailstones, should be considered when selecting measurement strategies for radar validation or model assimilation studies.

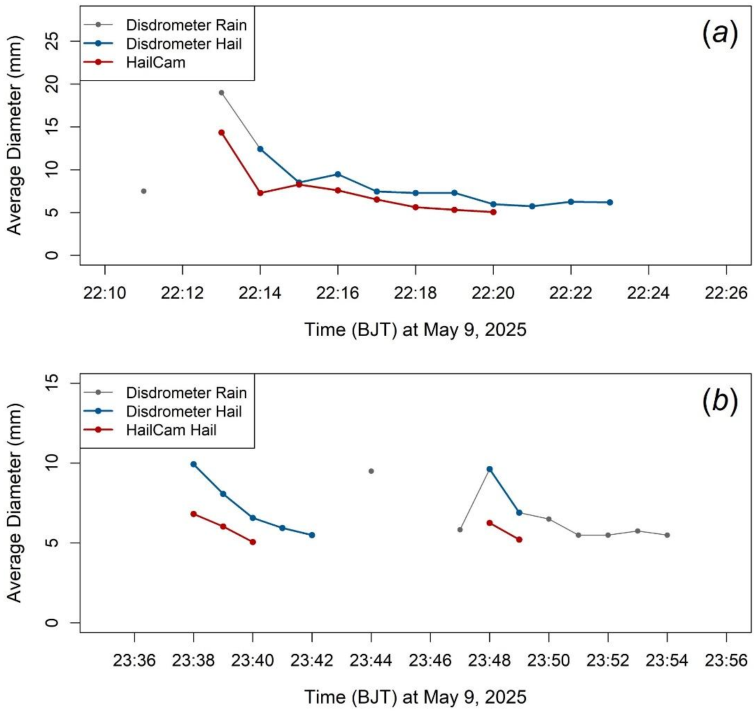

Figure 9: Temporal evolution of average particle diameter measured by HailCam (red) and the OTT Parsivel² disdrometer during two hail episodes on 9 May 2025. Particles with diameters ≥5 mm are considered. (a) First episode (22:13–22:20 BJT) and (b) second episode (23:38–23:49 BJT). Disdrometer measurements are separated into rain (grey circles) and hail (blue diamonds), while HailCam provides hail-only estimates (red circles with solid line). The time axis represents Beijing Time (BJT).

The temporal evolution of average particle diameter recorded by both instruments shows broadly consistent behavior across the two hail episodes (Figure 9). In both cases, the average hail diameter measured by HailCam decreases progressively as each episode unfolds, from 14.2 mm at 22:13 BJT to 5.1 mm at 22:20 BJT in the first episode, and from 6.8 mm at 23:38 BJT to 5.1 mm at 23:40 BJT for the first pulse and from 6.3 mm to 5.2 mm for the second pulse in the second episode. This pattern suggests a shift toward smaller hydrometeors, either through the preferential melting of larger hailstones during descent or the increasing dominance of smaller particles toward the end of the storm, consistent with the "size sorting" phenomenon observed in previous hail studies (Knight and Charles, 2010).

Despite this overall temporal coherence, notable quantitative differences emerge between the two instruments. During the early phase of the first episode (Figure 9a), HailCam reports substantially larger average diameters (14.2 mm at 22:13 BJT) compared to the disdrometer hail classification (12.3 mm at 22:14 BJT). This discrepancy likely stems from the disdrometer's velocity-based classification algorithm, which may misidentify large, irregularly shaped hailstones as raindrops or graupel due to anomalous fall velocities, whereas HailCam's imaging-based approach directly measures geometric dimensions regardless of particle density or shape. The disdrometer also identifies sporadic large raindrops (>15 mm) at 22:12 BJT, a signal absent in the HailCam record, further highlighting the instrument's focus on solid hydrometeors.

In contrast, the second episode (Figure 9b) exhibits closer quantitative alignment during the main hail phase (23:38–23:42 BJT), with both instruments capturing a decline from ~10 mm to ~5 mm. However, HailCam misses the brief hail pulse around 23:48 BJT detected by the disdrometer, likely due to the 60-second imaging duty cycle or particle overlap effects during this secondary intensity peak. This improved correspondence in the first half of the episode suggests that under more clearly defined hail conditions, with less contamination from heavy rain or mixed-phase particles, the two measurement approaches converge, reinforcing the reliability of HailCam for real-time hail monitoring when validated against established ground-based sensors.

Collectively, these observations demonstrate that HailCam not only provides accurate quantification of hailfall intensity but also captures the temporal evolution of particle size distributions—features essential for validating radar-based hail algorithms and improving convective-scale numerical models in complex terrain.

3.3 Uncertainty and Error Analysis

The hail observation system based on deep learning–driven image analysis demonstrates robust performance under field conditions; however, several interrelated sources of uncertainty must be carefully considered when interpreting the retrieved microphysical parameters. ~~First, instrumental~~

3.3.1 Instrumental and Algorithmic Uncertainties

Instrumental setup plays a critical role in measurement fidelity. Any deviation from perfect orthogonality between the collection surface and the imaging plane, such as platform tilt, camera misalignment, or incomplete field-of-view coverage, introduces geometric projection errors that systematically bias diameter estimates toward smaller values (detailed in the Text S2 in the supplementary material). This effect is particularly pronounced for particles near the edges of the imaging area, where perspective distortion is maximized. Consequently, rigorous installation protocols, including precise leveling of the collection tray, calibration of focal distance, and verification of uniform illumination across the entire active area, are essential to minimize spatially dependent biases and ensure consistent sizing accuracy.

~~Second~~Besides, algorithmic limitations inherent to the deep learning framework contribute non-negligible uncertainty. While the model achieves high detection recall under ideal conditions, it occasionally fails to identify hailstones that are small (<5 mm). Based on our validation against manual counts, the algorithm exhibits an average undercounting rate of 6.8%. This undercounting is primarily caused by the merging of adjacent or overlapping hailstones during image segmentation. Such missed detections lead to undercounting, which propagates into biases in derived quantities such as number concentration, cumulative flux, and mean particle size. Furthermore, the retrieval algorithm assumes spherical particle geometry to simplify volume and kinetic energy estimation, a reasonable approximation for small hail but increasingly inaccurate for larger, irregularly shaped stones commonly observed in severe storms. This shape simplification introduces systematic underestimation of true cross-sectional area and mass with assumed density, especially for fractured or conical hailstones.

~~Third, real~~3.3.1 Environmental and Natural Uncertainties

Real-world environmental dynamics introduce additional layers of uncertainty. During periods of intense hailfall, rapid accumulation can cause some particles to be mechanically displaced into the collection bin before imaging, decoupling optical counts from gravimetric measurements. Conversely, during relative warm hail-season, partial melting during the brief interval between impact and image capture reduces both apparent diameter and number, skewing size distributions toward smaller bins. Moreover, impacts from large hailstones can induce transient vibrations in the instrument housing, resulting in motion blur or frame jitter that degrades edge sharpness and compromises contour-based sizing.

Another unaccounted uncertainty source in static manual calibration is morphological distortion caused by terminal-velocity hail impacts on the collection grid. Natural hailstones fall with terminal velocities ranging from ~8 $m\ s^{-1}$ (5 mm hail) to >25 m s^{-1} (45 mm hail); high-energy vertical impacts can temporarily flatten oblate hailstones or split brittle ice particles into multiple fragments. The HailCam funnel buffer partially mitigates this by decelerating hydrometeors prior to contact with the imaging grid, and sub-5 mm shattered ice fragments drain through the grid mesh and are excluded from imaging. Even so, partial flattening of intact hailstones widens their projected horizontal silhouette, creating a small positive bias in equivalent diameter retrievals—an error mode entirely absent in our static manual placement calibration. This impact deformation bias is not quantified in the present laboratory tests and represents an uncharacterized field uncertainty term.

It also should be noted that over the 60-second accumulation window prior to imaging, newly arriving hailstones collide with particles already resting on the collection grid. These collisions can displace settled hailstones, chip small fragments off particle edges, or press adjacent hailstones into tighter overlapping clusters. Dense overlapping from collision aggregation worsens Mask R-CNN instance merging, exacerbating the undercounting bias observed at high particle densities (Section 3.1.2). The instrument supports flexible configuration of sampling intervals ranging from a maximum of 60 s down to a minimum of 20 s. Shortening the imaging cycle to 20 s drastically cuts the total volume of hailstones accumulated on the tray within each capture window, which markedly reduces the frequency of sequential inter-particle collisions and particle stacking during accumulation.

Collectively, these instrumental, algorithmic, and environmental factors define the current error characteristics of the system. Ongoing efforts focus on integrating multi-angle imaging, implementing real-time melt-correction models, and embedding physical constraints into neural network architectures to enhance robustness and reduce systematic biases in operational hail microphysical retrievals. Besides, to address the limitations of static manual calibration, a follow-up dynamic drop-test campaign would be helpful using a vertical fall tower capable of reproducing terminal fall velocities for 5–45 mm synthetic ice spheres, in order to develop a quantitative correction model for impact-induced sizing and counting biases to be integrated into the HailCam post-processing pipeline in future firmware updates.

4. Conclusion

In this study, we have presented HailCam, a deep learning-embedded hail observation instrument designed to address critical gaps in time-resolved, ground-based hail microphysics measurements. Through integrated high-definition imaging, automated sample collection, and edge-computing inference, the system delivers one-minute resolution data on hailstone number concentration, and size distributions, which are essential for validating radar-based hail algorithms and constraining numerical weather prediction models.

Multi-stage validation establishes key performance characteristics. Laboratory experiments demonstrate sizing accuracy of 91% within ±5% relative error across the 5-45 mm diameter range, with systematic negative bias (1.97–3.63%) attributable to contour detection limitations. Counting linearity exceeds 99.8% explained variance for particle densities spanning sparse to dense accumulations. Field evaluation reveals agreement with reference disdrometer measurements in temporal evolution and size distribution shape, despite expected discrepancies in absolute counts due to fundamentally different phase-discrimination principles. The imaging-based approach provides superior specificity for unambiguous solid-phase identification compared to velocity-based classification.

Several limitations warrant consideration. Geometric projection errors arise from non-orthogonal camera alignment. Occasional under-detection affects small (<5 mm). Environmental factors including pre-imaging particle displacement, partial melting under marginal thermal conditions, and motion blur from large-stone impacts contribute additional uncertainty. The 60-second duty cycle may miss sub-minute intensity fluctuations during rapidly evolving events. Rigorous installation protocols ensuring orthogonal imaging geometry and uniform illumination are essential for operational deployment.

The HailCam architecture establishes a foundation for scalable, high-fidelity hail monitoring networks. Deployment in radar validation campaigns and assimilation into convective-scale ensemble systems will quantify the observational impact on severe weather nowcasting. Extension to multi-sensor arrays with overlapping fields of view could enable three-dimensional hail trajectory reconstruction and microphysical process studies. The dataset from the Weining experimental campaign is publicly available to support community algorithm development and intercomparison initiatives.

Data availability

The ~~HailCAM~~HailCam and disdrometer data obtained from the Weining site are accessible at Zenodo (DOI 10.5281/zenodo.18585358).

Author contributions

BL: conceptualization, methodology, statistical and formal analysis, visualization, data curation, writing original draft, review, and editing. HW: conceptualization, methodology, data curation, writing and editing. TG: conceptualization, instrument deployment and maintenance, field campaign coordination. ZY: conceptualization, ground truth intercomparison design, review and editing. ZZ: Conceptualization, calibration protocol development, uncertainty analysis. YD: conceptualization, embedded system integration, real-time data transmission setup. YH: image preprocessing pipeline optimization, performance benchmarking. XL: conceptualization, project administration, funding acquisition.

Competing interests

The contact author has declared that none of the authors has any competing interests.

Financial support

This research was funded by the National Natural Science Foundation of China Project (42475208), Experimental Research on Hail Suppression Technology in Yunnan-Guizhou Plateau (ZQC-24447), Artificial Weather Modification Field Experiment, Technical Research, and Benefit Assessment Service Project of Yunnan Artificial Weather Modification Centre(ZDGL-W2024-004).

References

Allen, J. T., Giammanco, I. M., Kumjian, M. R., Jurgen Punge, H., Zhang, Q., Groenemeijer, P., Kunz, M., and Ortega, K. L.: Understanding Hail in the Earth System, Reviews of Geophysics, 58, 2020.

Barras, H., Hering, A., Martynov, A., Noti, P.-A., Germann, U., and Martius, O.: Experiences with >50,000 Crowdsourced Hail Reports in Switzerland, Bulletin of the American Meteorological Society, 100, 1429-1440, https://doi.org/10.1175/BAMS-D-18-0090.1, 2019.

Bhandari, S., Vajpayee, G., da Silva, L. L., Hinterstein, M., Franchin, G., and Colombo, P.: A review on additive manufacturing of piezoelectric ceramics: From feedstock development to properties of sintered parts, Materials Science and Engineering: R: Reports, 162, 100877, https://doi.org/10.1016/j.mser.2024.100877, 2025.

Changnon, S. A.: Hailstreaks, Journal of Atmospheric Sciences, 27, 109-125, https://doi.org/10.1175/1520-0469(1970)027<0109:H>2.0.CO;2, 1970.

Cheng, L. and English, M.: A Relationship Between Hailstone Concentration and Size, Journal of the Atmospheric

Sciences, 40, 204-213, 1983.

Dessens, J., Berthet, C., and Sanchez, J. L.: A point hailfall classification based on hailpad measurements, Atmospheric Research, 83, 132-139, 2007.

Dessens, J., Berthet, C., and Sanchez, J. L.: Change in hailstone size distributions with an increase in the melting level height, Atmospheric Research, 158-159, 245-253, 2015.

Federer, B. and Waldvogel, A.: Hail and Raindrop Size Distributions from a Swiss Multicell Storm, Journal of Applied Meteorology and Climatology, 14, 91-97, https://doi.org/10.1175/1520-0450(1975)014<0091:HARSDF>2.0.CO;2, 1975.

Fonseca-Cerda, M. d. S., de Moel, H., van Ederen, D., Schmid, T., Wouters, L., Aerts, J. C. J. H., Botzen, W. J. W., and Haer, T.: Hailstorm prediction and loss assessment using high-resolution hazard and claims data, Atmospheric Research, 329, 108501, https://doi.org/10.1016/j.atmosres.2025.108501, 2026.

Knight and Charles, A.: On the Mechanism of Spongy Hailstone Growth, Journal of the Atmospheric ences, 25, 440-444, 2010.

Kopp, J., Manzato, A., Hering, A., Germann, U., and Martius, O.: How observations from automatic hail sensors in Switzerland shed light on local hailfall duration and compare with hailpad measurements, Atmospheric Measurement Techniques, 16, 3487-3503, 10.5194/amt-16-3487-2023, 2023a.

Kopp, J., Schröer, K., Schwierz, C., Hering, A., Germann, U., and Martius, O.: The summer 2021 Switzerland hailstorms: weather situation, major impacts and unique -observational data, Weather, 78, 184-191, https://doi.org/10.1002/wea.4306, 2023b.

Li, Y., Mou, X., Kang, J., Zhu, S., Fan, Y., Fan, H., Wei, X., Chen, D., Ren, S., Jia, S., Li, J., Li, N., Ran, L., Zhou, K., and Zhang, J.: The Development of a Hailstone Disdrometer and Its Preliminary Observation in Aksu, Xinjiang, 10.3390/atmos15070823, 2024.

List, R., Cantin, J. G., and Ferland, M. G.: Structural Properties of Two Hailstone Samples, Journal of the Atmospheric Sciences, 27, 1080-1090, 2010a.

List, R., Rentsch, U. W., Byram, A. C., and Lozowski, E. P.: On the Aerodynamics of Spheroidal Hailstone Models, Journal of the Atmospheric Sciences, 30, 653-661, 2010b.

Liu, Z., Mao, H., Wu, C. Y., Feichtenhofer, C., Darrell, T., and Xie, S.: A ConvNet for the 2020s, 2022 IEEE/CVF Conference on Computer Vision and Pattern Recognition (CVPR), 18-24 June 2022, 11966-11976, 10.1109/CVPR52688.2022.01167,

Loffler-Mang, M. and Joss, J.: An Optical Disdrometer for Measuring Size and Velocity of Hydrometeors, Journal of Atmospheric & Oceanic Technology, 17, 130-139, 2000.

Löffler-Mang, M., Schön, D., and Landry, M.: Characteristics of a new automatic hail recorder, Atmospheric Research, 100, 439-446, https://doi.org/10.1016/j.atmosres.2010.10.026, 2011.

Martius, O., Hering, A., Kunz, M., Manzato, A., Mohr, S., Nisi, L., and Trefalt, S.: Challenges and Recent Advances in Hail Research, Bulletin of the American Meteorological Society, 99, ES51-ES54, https://doi.org/10.1175/BAMS-D-17-0207.1, 2018.

Mroz, K., Battaglia, A., Lang, T. J., Cecil, D. J., Tanelli, S., and Tridon, F.: Hail-Detection Algorithm for the GPM Core Observatory Satellite Sensors, Journal of Applied Meteorology & Climatology, JAMC-D-16-0368.0361, 2017.

Nisi, L., Hering, A., Germann, U., and Martius, O.: A 15-year hail streak climatology for the Alpine region, Quarterly Journal of the Royal Meteorological Society, 144, 1429-1449, https://doi.org/10.1002/qj.3286, 2018.

Pflaum, J. C.: New Clues for Decoding Hailstone Structure, Bulletin of the American Meteorological Society, 65, 1984.

Pilorz, W., Zięba, M., Szturc, J., and Łupikasza, E.: Large hail detection using radar-based VIL calibrated with isotherms from the ERA5 reanalysis, Atmospheric Research, 274, 106185, https://doi.org/10.1016/j.atmosres.2022.106185, 2022.

Punge, H. J. and Kunz, M.: Hail observations and hailstorm characteristics in Europe: A review, Atmospheric Research, 176-177, 159-184, https://doi.org/10.1016/j.atmosres.2016.02.012, 2016.

Raupach, T. H., Martius, O., Allen, J. T., Kunz, M., Lasher-Trapp, S., Mohr, S., Rasmussen, K. L., Trapp, R. J., and Zhang, Q.: The effects of climate change on hailstorms, Nature Reviews Earth & Environment, 2, 213 - 226, 2021.

Ravinder, A., Reddy, P. K., and Prasad, N.: Detection of Wavelengths for Hail Identification Using Satellite Imagery of Clouds, IEEE Computer Society, 2013.

Sánchez, J. L., Gil-Robles, B., Dessens, J., Martin, E., Lopez, L., Marcos, J. L., Berthet, C., Fernández, J. T., and García-Ortega, E.: Characterization of hailstone size spectra in hailpad networks in France, Spain, and Argentina, Atmospheric Research, 93, 641-654, 2009.

Skripnikova, K. and Rezacova, D.: Radar-based hail detection, Atmospheric Research, 144, 175-185, 2014.

Smyth, T. J., Blackman, T. M., and Illingworth, A. J.: Observations of oblate hail using dual polarization radar and implications for hail-detection schemes, Quarterly Journal of the Royal Meteorological Society, 1999.

Soderholm, J. S., Kumjian, M. R., Mccarthy, N., Maldonado, P., and Wang, M.: Quantifying hail size distributions from the sky – application of drone aerial photogrammetry, Atmospheric Measurement Techniques, 13, 747-754, 2020.

Tokay, A., Wolff, D. B., and Petersen, W. A.: Evaluation of the New Version of the Laser-Optical Disdrometer, OTT Parsivel2, Journal of Atmospheric and Oceanic Technology, 31, 1276-1288, https://doi.org/10.1175/JTECH-D-13-00174.1, 2014.

Wang, P. K., Greenwald, T. J., and Wang, J.: A Three Parameter Representation of the Shape and Size Distributions of Hailstones—A Case Study, Journal of Atmospheric Sciences, 44, 1062-1070, https://doi.org/10.1175/1520-0469(1987)044<1062:ATPROT>2.0.CO;2, 1987.

Wobrock, W., Flossmann, A. I., and Farley, R. D.: Comparison of observed and modelled hailstone spectra during a severe storm over the Northern Pyrenean foothills, Atmospheric Research, 67, 685-703, 2003.